The vertical distribution of biomass burning pollution over tropical South America from aircraft in situ measurements during SAMBBA

Eoghan Darbyshire[1], William T. Morgan[1], James D. Allan[1], Dantong Liu[1], Michael J. Flynn[1], James R. Dorsey[1], Sebastian J. O'Shea[1], Douglas Lowe[1], Kate Szpek[2], Franco Marenco[2], Ben. T. Johnson[2], Stephane Bauguitte[3], Jim M. Haywood[2,4], Joel F. Brito[5*], Paulo Artaxo[5], Karla M. Longo[6**], Hugh Coe[1]

[1]Centre for Atmospheric Science, University of Manchester, Manchester, UK
[2]Met Office, Exeter, UK
[3]Facility for Airborne Atmospheric Measurements (FAAM), The University of Cranfield, Cranfield, UK
[4]CEMPS, University of Exeter, Exeter, UK
[5]Physics Institute, University of Sao Paulo, Sao Paulo, Brazil
[6]National Institute for Space Research (INPE), Sao Jose dos Campos, Brazil
*Now at Laboratory for Meteorological Physics (LaMP), University Clermont Auvergne, Aubière, France
**Now at NASA Goddard Space Flight Center and USRA/GESTAR, Greenbelt, MD, USA

Correspondence to: Eoghan Darbyshire (eoghan.darbyshire@manchester.ac.uk)

Abstract.

To reduce the uncertainties in processes driving the vertical distribution of biomass burning pollutants, and thus impacts on regional weather and climate, we present an integrated analysis of vertical profiles of pollutants and meteorological parameters measured on flights during the 2012 South American Biomass Burning Analysis (SAMBBA) field experiment.

During the dry season there were significant contrasts in the composition and vertical distribution of haze between western and eastern regions of tropical South America. Owing to an active or residual convective mixing layer, the aerosol burden was similar from the surface to ~1.5 km in the west and ~3 km in the east. Black carbon mass loadings were double in the east (1.7 µg cm^{-3}) than west (0.85 µg cm^{-3}) but aerosol scattering coefficients at 550 nm were similar (~120 Mm^{-1}), as too were CO surface concentrations (310-340 ppb). We attribute these contrasts to the more flaming combustion of Cerrado fires in the east and more smouldering combustion of deforestation and pasture fires in the west. Horizontal wind shear was important in inhibiting mixed layer growth and plume rise, in addition to advecting pollutants from the Cerrado regions into the remote tropical forest of central Amazonia. Optically thin layers above the mixing layer indicates roles for both plume injection and shallow moist convection in delivering pollution to the lower free troposphere. However, detrainment of large smoke plumes into the upper free troposphere was very infrequently observed. Our results reiterate that thermodynamics control the pollutant vertical distribution and thus point to the need for correct model representation so the spatial distribution and vertical structure of biomass burning smoke is captured.

Our observations of relatively large concentrations of aerosol aloft and of CO near surface suggest that there is a greater contribution of pollutants from more complete combustion with altitude. Release of appropriate emissions from the initial more flaming and later residual smouldering phases of a fire at appropriate altitudes may be especially important to ensure models can accurately predict aerosol-radiation, aerosol-cloud and air quality impacts.

1 Introduction

The vertical distribution of biomass burning pollution influences its impacts on weather (e.g. Kolusu et al., 2015), climate (e.g. Boucher et al., 2013), human health (e.g. Reddington et al., 2015) and ecosystem function (e.g. Rap et al., 2015). The vertical location of aerosol is particularly sensitive since this can impact radiative forcing (Zarzycki and Bond, 2010), alter cloud microphysics (Tao et al., 2012) and feedbacks on cloud dynamics (Feingold et al., 2005). The altitude of pollutants also determines their atmospheric residence time, which will affect any ageing processes and the resultant horizontal distribution following advection. Model predictions of the vertical distribution of the effects of biomass burning smoke are therefore very dependent on accurately capturing the vertical structure, especially in regions of the tropics where land use change is rapid and smoke is widely distributed. However, a lack of detailed observations across these regions limits model constraint.

These uncertainties are pronounced in tropical South America (TSA), one of the largest global biomass burning sources. Aerosol accumulates within the convective boundary layer forming a regional haze with a lifetime of 4-5 days (Edwards et al., 2006) that can cover up to 6 million km^2 (Prins et al., 1998) and reach aerosol optical depths (AOD) of up to 4 in the mid-visible during particularly polluted years (Artaxo et al., 2013). Fires are widespread within the so-called 'arc of deforestation' which traverses the southern and eastern edges of the Amazon basin. This arc comprises both tropical forest rainforest and Cerrado (savannah-like) biomes which feature distinct fire regimes.

Previous studies have discussed the vertical distribution of biomass burning pollutants in TSA based on in situ aircraft measurements. The 1985 ABLE-2B study across northern Amazonia from the coast to Manaus provided profiles and transects of aerosol extinction (Andreae et al., 1988) , CO (Sachse et al., 1988), aerosol number and ozone (Gregory et al., 1988). The 1992 TRACE-A campaign in central and eastern TSA yielded vertical profiles of total aerosol and black carbon mass (Pereira et al., 1996). The 1995 SCAR-B and 2002 LBA-SMOCC studies focused on western TSA, providing vertical information on aerosol number (Andreae et al., 2004), aerosol scattering (Chand et al., 2006; Ross et al., 1998) and CO concentrations (Freitas et al., 2009). The 2004 TROFFEE campaign in central TSA provided vertical profiles of CO and CO_2 (Yokelson et al., 2007). Finally, the 2009 BARCA-A study provided aerosol number and CO concentrations in central and northern TSA (Andreae et al., 2012). Common among these studies is the limited regional spatial extent and the coverage above ~4 km, whilst many only show singular profiles and/or do not consider the eastern Cerrado fire regime. Furthermore, profiles are typically not integrated with multiple pollutants nor simultaneous thermodynamic measurements. This is important for understanding how mixing, advection and removal affect pollutants differently. Likewise, recent lidar remote sensing from satellite (Bourgeois et al., 2015; Huang et al., 2015) and surface (Baars et al., 2012) platforms do not provide the comprehensive dataset best suited to examining the drivers of multi-pollutant vertical distribution.

When simulating the pollutant vertical distribution over TSA there is a large diversity between AeroCom global models (Koffi et al., 2012) and between a subset of regional models (Andreae et al., 2012). In particular, open questions remain regarding treatment of convective mixing (Archer-Nicholls et al., 2015) and the injection of buoyant plumes into the vertical column (Paugam et al., 2016). Furthermore, to ensure consistency with remotely sensed AOD measurements, emissions are

typically up-scaled by a factor of two to five (Johnson et al., 2016; Reddington et al., 2016). There is no established physical understanding of this requirement, with deficiencies in both emissions inventories and model process posited. As such, scaling factors represent a key uncertainty in model treatment of biomass burning across the globe.

In this study we examine the key controls on the vertical distribution of biomass burning pollution across TSA during the 2012 dry season using data collected on research flights during the SAMBBA (South AMerican Biomass Burning Analysis) field experiment. This study includes the first incandescence based measurements of black carbon mass and mixing state in a tropical biomass burning region, and also the most comprehensive integrated multi-parameter library of profiles for tropical South America. It also represents the first comprehensive airborne sampling in eastern Cerrado regions of intensive fire activity. To determine the key drivers of pollutant distribution we examine: features of the atmospheric structure (Sect. 3.1); their interaction with pollutants based on a novel and detailed analysis of individual profiles (Sect. 3.2); and, fire activity and horizontal aerosol distributions based on satellite observations (Sect. 3.3). Average pollutant profiles are presented across the different synoptic regimes over TSA (Sect. 3.4). Together, these approaches allow determination of the key drivers of the vertical distribution of biomass burning pollution, and an examination of how these manifest in different environments and relate to previous observations (Sect. 4). A discussion of implications and recommendations for future measurement and model approaches to reduce the uncertainty surrounding the impacts of biomass burning pollution both in TSA and other tropical biomass burning regions is presented (Sect. 5).

2 Experimental details

Twenty science flights were conducted during the SAMBBA experiment between 14th September and 3rd October 2012, primarily based out of Porto Velho in northern Rondônia state, Brazil (Fig. 1). Extensive geographical sampling was conducted via three basic flight operations: (i) straight and level runs within the boundary layer, (ii) high altitude surveys and (iii) profile ascents/descents. Flights were conducted by the UK BAe-146 research aircraft operated by FAAM (Facility for Airborne Atmospheric Measurements). The BAe-146 flew with a comprehensive instrumentation suite, capable of measuring aerosols, dynamics, cloud physics, chemical tracers and meteorological fields (McBeath, 2014). Simultaneously, a fully instrumented ground site was operational in Porto Velho, the results from which are described in Brito et al. (2014).

Aerosol total scattering coefficients were measured by a 3-wavelength integrating nephelometer (TSI Inc., USA; Anderson et al., 1996). Standard corrections were applied for angular truncation and non-Lambertian light source errors (Anderson and Ogren, 1998; Müller et al., 2011). The total scattering coefficient at 550 nm is reported at either dry RH (<30%), σ_{sp_dry}, or ambient RH, σ_{sp_amb}. These values were derived from the measured data based on the internal RH of the nephelometer and applying humidification scaling factors from Fig. 4c of Kotchenruther and Hobbs (1998). Note, however, there remains significant uncertainty on the role of water uptake on aerosol in TSA (Reddington et al., 2018, Darbyshire et al., in preparation).

Mass concentrations of refractory Black Carbon (rBC) were obtained using the Single Particle Soot Photometer (SP2, Droplet Measurement Technologies, USA; Baumgardner et al., (2004), Stephens et al., (2003)). The operation on board the

BAe-146 is outlined by McMeeking et al. (2010) and the calibrations and post processing undertaken for this work are described by Allan et al. (2014). Reported mass loadings have a measurement uncertainty of approximately 30% (Schwarz et al., 2008; Shiraiwa et al., 2008). The coating thickness of scattering material on core rBC particles was calculated following the method presented by Liu et al. (2014) and Taylor et al. (2015). By assuming a full concentric encapsulation of the spherical core, the coating thickness of single rBC particles are estimated using a core refractive index of 2.26-1.26i and coating refractive index of 1.50+0i (Taylor et al., 2015).

The SP2 and nephelometer sampled through a Rosemount inlet which has a high transmission for the submicron aerosols presented here (Trembath, 2013). rBC and σ_{sp} are reported at standard temperature (273.15 K) and pressure (1013.2 hPa) to allow direct comparison of particle composition at different altitudes.

Carbon dioxide mixing ratios were measured by a fast greenhouse gas analyser (FGGA; Los Gatos Research Inc.) adapted for aircraft use (O'Shea et al., 2013). The total accuracy of this measurement is estimated at ±0.17 ppm. Carbon monoxide mixing ratios were measured by an Aero-Laser AL5002 VUV resonance fluorescence gas analyser (Gerbig et al., 1999). Total uncertainty of the FAAM instrument is estimated to be ±2% (O'Shea et al., 2013). In flight calibrations were performed for CO and CO_2 using World Meteorological Organization traceable gas standards.

A General Eastern 1011B (GE Measurement & Control) chilled mirror hygrometer provided measurements of ambient dew point temperature, accurate to ±0.2 ∘C. A Rosemount/Goodrich type-102 True Air Temperature sensor was mounted outside the aircraft, providing ambient temperature measurements using a Rosemount 102AL platinum resistance immersion thermometer. A total of 56 Vaisala RD94 dropsondes were released from the aircraft at altitudes up to 8 km, providing geolocated profiles of pressure, temperature, relative humidity and wind vectors to ground level.

Individual profiles were averaged (median) onto a 50 m vertical grid for automated identification of thermodynamic features and their relation to haze distribution and pollutant plumes. Plumes identified on take-off/approach to an airport were removed from further analyses as they were likely contaminated from urban emissions.

Satellite remote sensing products were obtained for the SAMBBA period and September 2008-2017. The MODIS (Moderate Resolution Imaging Spectroradiometer) instrument provided retrievals of aerosol optical depth and active fire data. Precipitation rates were acquired from instruments on-board TRMM (Tropical Rainfall Measuring Missions). Land cover data was acquired from the ESA CCI Land Cover project and used the United Nations Land Cover Classification System. Specific details on the acquisition and processing of satellite data are provided in the supplement.

3 Results

3.1 Atmospheric structure

The evolution of the convective boundary layer is important for pollutant mixing, advection and plume injection and is idealised in Fig. 2. Surface heating initiates buoyant turbulent motions which deepen throughout the day and comprise the convective mixing layer. In the morning these thermals slowly destabilise the nocturnal stable layer before rapidly penetrating

into the residual layer, i.e. the previous days' boundary layers. Growth of the mixed layer is inhibited by the statically stable entrainment zone, a region of overshooting thermals and downward entrainment from above. The lifting condensation level is typically within the entrainment zone but above the mixed layer top, leading to patchy cumulus fields. These clouds are either forced, i.e. fair weather cumulus which do not vent mixing layer air into the free troposphere, or active, where the level of free

5   convection is reached and mixing layer air is vented through the tops of towering cumulus that may grow up to the limit of convection and detrain in the upper troposphere (Stull, 1985). Typically, a maximum in horizontal wind speed of variable magnitude and extent is present above the entrainment zone.

     The layer altitudes in Fig. 2 are based on a semi-automated analysis of individual thermodynamic profiles, the methodology for which is detailed in Sect. S2. This analysis is summarised for an example profile in Fig. 3A-C. From the wind speed and

10   direction profiles (panel A), regions of local positive wind shear (vertical brown line) and locations of wind speed maxima (open purple circles) are identified. Profiles of relative humidity, specific humidity, potential temperature and equivalent potential temperature (panel B) act as the basis for identification of a mixed layer and where so, its depth. This involved a manual approach based on the spread of a number of automated methods. Profiles of temperature and dew point temperature (panel C) are presented in a skew-T log-P format, allowing calculation of the lifting condensation level (LCL), level of free

15   convection (LFC) and limit of convection (LOC). The entrainment zone was not derived due to difficulties in determining its base with the information available. The format of Fig. 3 is replicated for each profile and displayed in Sect. S5.

     In general, observed profiles of horizontal wind speed reflect those expected based on our understanding of synoptic flows over TSA. In the lower troposphere (850 hPa) the mean synoptic circulation is an anticyclonic flow centred around south eastern TSA: easterly trade winds turn south-eastward toward the extra tropics, parallel to the Andes (Fig. 4C). Horizontal

20   wind speed is greatest along eastern coastal regions, northern Amazonia and Bolivia, whilst slacker wind speeds are prevalent in south western TSA. At higher levels the influence of the Andes is reduced, resulting in a more zonal flow.

     There is considerable structure in the observed profiles which is not captured by large scale wind fields, such as those in the ECMWF ERA-Interim reanalysis. This includes multiple filament like maxima in wind speed, often without accompanying changes in wind direction. In western TSA the expected sharp change in wind direction and increase in horizontal wind shear

25   associated with a trade wind inversion is often not present and instead a more gradual change in speed and direction was observed. In the mixed layer, horizontal wind speed is typically lower and of a more uniform direction and magnitude. There are a number of exceptions to this generalisation, where positive wind shear regions or wind speed maxima are present through the mixed layer. A wind speed maximum is generally observed above or collocated with the mixed layer top (e.g. Fig. 3). If this feature is associated with a region of positive wind shear below, mixed layer growth is likely inhibited and in turn the

30   magnitude of the jet and gradient of wind shear reduces.

     Variations of the Fig. 2 idealised structure were also found to depend on the sample region, owing to the west-east asymmetries in land use. Compared to the Cerrado regions, the northern and western tropical forest regions experience higher levels of precipitation, soil moisture and cloud fraction resulting in lower solar insolation and surface temperatures (Fig. S2). On average these resulted in a deeper, faster developing, mixing layer in the east than west and north (average of 1.8 km vs.

1.1 km). As such the lifting condensation level (2.6 km vs. 1.4 km) and level of free convection (3.1 km vs 2.4 km) was also greater. Only in 25% of profiles was the limit of convection identified, where it was higher in the east than west and north (4.4 km vs. 3.5 km).

Superimposed on the regional variation was the impact of two distinct meteorological phases in north and west TSA. Between 14-Sept and 22-Sept conditions were characteristic of the dry season, whilst between 23-Sept and 05-Oct conditions more closely resembled those of monsoonal transition (Brito et al., 2014). This second phase was characterised by an increased rate and area of rainfall, accompanied by reductions in solar insolation and increases in cloud fraction and soil moisture (Fig. 4). In ~30% of profiles no mixing layer could be identified and instead the lower atmosphere was conditionally unstable throughout (and hence Fig. 2 is unrepresentative). This typically occurred in the west of TSA and toward the end of the campaign as wet season type conditions became more prevalent. Meteorological conditions during the 2012 SAMBBA period were typical of the climatology – there were no climatic extremes (Fig. S2).

3.2 Determining pollutant vertical distribution via feature analysis of individual vertical profiles

An automated analysis of interactions between atmospheric structure and pollutant burdens was undertaken for each individual profile. Results from this analysis are summarised in Table S1 and illustrated for the example profile in Fig. 3D-G. The full analysis methodology is provided in Sect. S2.

When present, the convective mixing layer was investigated to determine if each pollutant was correspondingly well mixed throughout the layer. This is the case in approximately half of all profiles featuring a mixed layer. The profiles where this was not the case are typically perturbed by fresh plumes and/or wind shear and jet interactions. The number of CO and CO_2 profiles taken during the morning that were classified as well mixed was approximately half that of the afternoon. For example in Fig. 3 - as indicated by the vertical green line and accompanying yes/no indicator - rBC and σ_{sp_dry} are considered well mixed but CO and CO_2 are not, due to concentrations increasing near the surface.

If pollutant burdens in the region above the mixing layer (or if absent, the surface) and 4 km exceeded those of unpolluted background conditions, a pollutant residual layer was identified. Dry season background conditions were defined as 0.1 µg cm^{-3} for rBC (Artaxo et al., 2013), 15 Mm^{-1} for σ_{sp} (Rizzo et al., 2013) and 140 ppb for CO (Andreae et al., 2012). Since CO_2 has significant global trends and the large biogenic sources/sinks its background is harder to quantify and is not considered here. Over 80% of profiles included a pollutant residual layer, even those in remote regions away from fresh emissions. Typically, the shape of these residual layers is similar to that from the previous day(s) boundary layer. However there is substantial diversity in shape and magnitude, especially between 2 - 4 km that result from variations in plume injection, long range transport, cloud detrainment or entrainment of clean air from aloft. This is seen in the profiles in Fig. 3 where the residual layer is indicated by the vertical brown line and accompanying yes/no indicator.

Two impacts of horizontal wind shear on pollutant vertical structure were explored. Firstly capping effects, indicated by a decline in pollutant burdens over regions of positive horizontal wind shear. This was present in 40-60% of instances. Secondly the curtailment by wind shear on plume rise via increased drag and lateral entrainment, as previously explored by Freitas et al.

(2010). This was indicated by a co-location of pollutant burden maxima with wind shear maxima. This was present in 20-30% of instances. Fig. 3 contains such an example at ~650 hPa, as illustrated by the purple circle in panel F.

Plumes were identified by a significant enhancement in pollutant burden (dot-dash grey lines, Fig. 3.D-G) over a local background (dashed grey lines, Fig. 3.D-G). The majority of profiles contain a plume of one or more pollutant. Only in 10% of these plumes did all pollutant burdens exceed the identification threshold, despite often being well correlated, indicating variability in plume composition. The plumes observed in the mixing layer are likely more fresh and locally injected. Their frequency increases in the afternoon (Table S2) which may be associated with increased fire incidence (Giglio et al., 2006). Plumes were encountered between the mixing layer and lifted condensation level in 15-20% of profiles, indicating a significant number of fire plumes have sufficient energy to overcome the stable entrainment zone. If the pyro-convection is such that the plume reaches above the lifted condensation level, as in 10-25% of profiles, pyro-cumulus form and detrain pollutants. Plumes encountered at these levels likely include those from local sources and those advected from regional upwind sources. The frequency of these plumes generally declines in the afternoon indicating pollutants have been re-entrained into the mixing layer or, in western regions, transported following deep moist convection above our flight ceiling.

It is possible the layers of enhanced pollutants above the lifting condensation level are not direct plume injections but detrainment from active cumuli following shallow moist convection. However, mixing layer pollution transported in this manner will be of similar concentrations to that of the residual layer and as such may not be significant enough to trigger the plume thresholds defined here. Furthermore it would be expected that relative concentrations of CO would be conserved but those of aerosol would be reduced following activation and wet scavenging if precipitation occurred. However, analysis of the plume composition (Sect. 3.4) indicates the opposite to be true. Together this indicates the pollutant enhancements observed here are likely plumes rather than detrained layers, although moist shallow convection is still likely important in transporting mixing layer air aloft. In the subset of profiles where the limit of convection was within the flight envelope only a couple of plumes were identified.

3.3 Fire activity

During the dry season fires are prevalent across TSA but especially between 0 and 25°S (Fig. 5A). Pollutants emitted from these fires accumulate in south-western TSA as the Andes act as a barrier to smoke advected westward via the trade winds (Fig. 5C). This regional smoke plume is optically thick and its shape and magnitude are dependent on fire activity in a given year. Whist the September 2012 dry season is generally representative of years since 2008 (Fig. 5A-C ii.), fire count and radiative power were greater in the eastern states. This likely explains the enhanced AOD of ~0.1 in these regions and southern Mato Grosso state. The shift to wet season conditions corresponded to a reduction in fire count (Fig. 6A) and emissions (Pereira et al., 2016). In northern, western and central regions we speculate this is likely due to a reduced ignition probability and the dampening or extinction of existing burns. The reduction in fire count and intensity in eastern regions occurred despite no significant change in precipitation. We speculate this may result from stronger easterlies (Fig. 4C.iii) inhibiting fire ignition

and spread. Together with increased wet removal, these effects acted to decrease the regional AOD by ~0.2 and shift the peak AOD from central to north eastern regions (Fig. 6C).

3.4 Vertical distribution of pollution over synoptic scales

Based on the variability between the individual profiles and the regional differences in fire activity, land use and meteorology, we define four regimes which characterise the key synoptic differences in pollutant burden and vertical distribution across TSA during SAMBBA:

- − Deforestation impacted western Amazonia around Rondônia and Mato Grosso states (68.5°W - 54°W, 12°S - 5.5°S) during dry season conditions (14-Sept to 22-Sept). This regime is henceforth referred to as W1.
- − The same area during dry-wet transition season conditions (23-Sept to 05-Oct). Henceforth W2.
- − 'Pristine' rainforested area north of Manaus (65°W - 59°W, 5.5°S - 1°S) during the dry season. Henceforth N1.
- − The dry Cerrado environment in eastern regions around Tocantins state (53°W - 46°W, 12°S - 9°S). Henceforth E0.

The geographic extent of these regimes is demonstrated in Fig. 1 and the median thermodynamic variables in Fig. 7.

The average aerosol vertical profile shapes of W1, W2 and N1 are similar (Fig. 8.A,B) - similar loadings occur from the surface to 3 km with a small maximum between 1 and 2 km. Above 4 km, loadings decline to near background values. Comparatively, E0 is characterised by a near surface maximum, which may be because multiple fresh fires were sampled, followed by similar loadings up to 4 km, above which concentrations declined sharply to near zero. The shape of the aerosol profiles is not affected if plumes are removed from the analysis.

There are also contrasts in the absolute aerosol burden between the regimes. There is a twofold reduction throughout the column between W1 and W2, consistent with the satellite AOD fields (Fig. 6). Within the boundary layer this represents a reduction from 0.85 to 0.4 µg cm^{-3} for rBC and 115 to 60 Mm^{-1} for σ_{sp_dry}. rBC loadings of 0.85 µg cm^{-3} in N1 are similar to those in W1, yet σ_{sp_dry} of 70 Mm^{-1} are more akin to W2. E0 features a similar ratio between rBC and σ_{sp_dry} as N1, although the burden is much larger at 1.7 µg cm^{-3} and 125 Mm^{-1}.

For all regimes CO mixing ratios are greatest at the surface: 340 ppb in W1, 310 ppb in E0, 220 ppb in W2 and 150 ppb in N1. CO mixing ratios reduce with altitude to a minimum in the free troposphere: 125 ppb at an unknown altitude in W1, 95 ppb at 4-5 km in E0, 150 ppb at 4-5 km in W2, 100 ppb at 3-4 km in N1, and. The reduction of CO mixing ratios in the boundary layer from W1 to W2 corresponds to that of the aerosol burden. CO_2 mixing ratios are also greatest at the surface: 402 ppm in E0, 393 ppm in N1, 394 ppm in W1 and in W2, where the surface enhancement is particularly prominent, 397 ppm. CO_2 mixing ratios also reduce with altitude with minima of 391 ppm in E0 and N1 or 392 ppm in W1 and W2 at the same altitudes as those for CO.

Profiles of pollutant ratios further illustrate the contrasting aerosol and gas phase vertical distributions (Fig. 9.A-B). Compared with CO and CO_2 the aerosol burden is enhanced at higher altitudes in the boundary layer, even accounting for the removal of plumes (Fig. S3). The peak enhancement is at ~2 km in W2, ~1.5 km in N1, ~4 km in E0 and, in W1, ~2.5 km for

σ_{sp_dry} and ~1.5 km for rBC. These distributions may be explained by the pollutant ratios within plumes - as altitude increases so does the plume Δaerosol:ΔCO ratio (Fig. 9.C-D).

There is limited evidence for a diurnal variation in aerosol burden and vertical profile shape. CO, however, is enhanced near the surface in the morning (Fig. 8). In W2 and N1, CO_2 is also enhanced at the surface in the morning but, given the poor
5   correlation with other pollutants (Sect S5), likely arises from biogenic activity. This may also help explain the greater CO_2 mixing ratios in W2 vs. W1, as the increased cloud cover reduces photosynthesis and hence CO_2 uptake (Graham et al., 2003).

Within the boundary layer there is a significant contrast in the coating thickness of rBC between E0 (55 nm) and W1, W2 and N1 (80-90 nm; Fig. 10, Fig. S4). Coating thickness increases with altitude in the boundary layers of W2, N1 and E0. This may be associated with partitioning of organic material into the particle phase as temperatures decrease, and/or the greater
10 prevalence of fresh emissions near surface. In W1, W2 and most markedly N1, the rBC coating thickness declines above the boundary layer. Comparatively, rBC coating thickness increases above the boundary layer in E0.

4 Discussion

4.1 Drivers of the pollutant vertical distribution

Fire class determines the relative mix of pollutants emitted. In E0 there are relatively greater loadings of rBC owing to
15 emissions from more efficient flaming combustion in Cerrado fires as observed by Hodgson et al. (2018). In W1 and W2 there are relatively greater magnitudes of σ_{sp_dry} and CO as the higher biomass density and moisture content results in more inefficient smouldering combustion. Significantly, the shift in meteorology between these two phases does not substantially impact the relative abundances of rBC, σ_{sp_dry} and CO.

Meteorological conditions determine the absolute pollutant concentrations via their impact on removal rates/processes,
20 advection and fire incidence. The driest conditions and greatest fire incidence meant the greatest pollutant concentrations were observed in E0. The reduction in aerosol loadings from W1 to W2 is attributable to a corresponding decline in fire count and increase in wet removal associated with the more widespread and heavy precipitation. Aside from wet removal, the ubiquity of the pollutant residual layer indicates pollutants are not rapidly removed. As such, advection becomes a key modulator of pollutant concentrations local to, and distant from, the source region. The latter is the case in N1 - back trajectory analysis
25 (Fig. S5) shows that pollutants are advected from the fire hotspot around Maranhão and northern Pará states (Fig. 5). The pollutant mix - relatively greater concentrations of rBC and – is consistent with the Cerrado burns at these sources. Whilst CO_2 mixing ratios are also greater in the east (relative to CO), as would be expected from more flaming combustion, the role of fire emissions cannot be evaluated given the confounding influence from biogenic sources/sinks in both regions.

The shapes of pollutant vertical distributions are primarily controlled by meteorological conditions, in particular vertical
30 convective motions and horizontal wind shear (Fig. 7). The former acts to mix pollutants released near the surface toward the mixing layer top, the altitude of which can be modulated by the latter, soil moisture and solar insolation. The difference in profile shape from west to east to north is primarily driven by contrasting mixed layer depths. Large unmixed plumes perturbed

this state, although contribute only 15% (E0), 11% (W1), 8% (W2), and 1% (N1) to the scattering only column AOD (calculated from the nephelometer, Sect. S2). Such plumes were seldom seen above 4 km, in contrast to previous observations in the region (Andreae et al., 2004), indicating the mass flux from large pyrocumulus detrainment into the upper troposphere (within the aircraft range) was not significant. A number of profiles show dilute layers above ~4 km indicating there may be

5   some vertical transport of mixing layer pollution into the free troposphere via shallow moist convection, although this feature is not widespread and is optically thin. Pollutant loadings were still relatively high above the mixing layer, indicating wet removal is not significant in the region. It was not possible to attribute the relative contributions to this burden from the previous day's mixing layer, long range transport and shallow moist convection. However, of the rBC present at these altitudes, coating thicknesses are smaller in the west and north, although exhibit significant variability. This is consistent with observations in

10   Boreal Canada of preferential wet deposition of the largest and most coated particles (Taylor et al., 2014).

Fig. 11 summarises the meteorological drivers of the east to west contrast in pollutant vertical distribution. A declining mixing layer depth from east to west is evident from the reduction in altitude of the sharp gradient (i.e. the entrainment zone) of θ_e from ~3 km in the eats to ~1.5 km in the west. Above the mixed layer top relative humidity increases, especially so after the lifted condensation level where the high humidity distinguishes the cloud convective layer. This layer is deeper in the west,

15   associated with deeper moist convection. A wind speed maximum is present at 5-6 km, coincident with the entrainment zone. Together, this structure can explain the lidar derived extinction coefficient distribution (first published by Marenco et al., 2016). Aerosol is capped below the first wind speed jet, well mixed within the mixed layer and features a maximum at ~1.5-2 km. Visible plumes at ~59 °W and ~52.5 °W lie at injection heights typical of those observed in the in situ profile data. The similarity of the in situ σ_{sp_amb} and lidar extinction coefficient profile shapes at the regional (Fig. 11) and local (Fig. S6) scales

20   engenders confidence in the representativity of both datasets. Disparity in the absolute magnitudes is primarily explainable by differences in the sampling coverage (Fig. S7).

Plume injection altitude is potentially significant in driving the contrasting vertical distributions between different pollutants in all regimes. We observe the relationship between Δaerosol:ΔCO and altitude is driven by plumes at higher altitude being enriched in aerosol and at low altitudes enriched in CO. We speculate the plumes at higher altitude arise from fires with

25   more efficient combustion and at lower altitudes from less efficient combustion. This is consistent with the relationship described between combustion efficiency and Δaerosol:ΔCO from previous observations in the region (Fig. S8; Ferek et al., 1998; Yokelson et al., 2007) and SAMBBA (Fig. S9, Hodgson et al. 2018). Previous studies of biomass burning plumes have described the relationship between combustion completeness phase plume injection height (Akagi et al., 2011; Freitas et al., 2006). As such, we postulate the enhanced aerosol at altitude is due to lofted emissions from more flaming combustion, and

30   the reduced aerosol near surface results from a dominance of smouldering emissions. CO near surface enhancements in the morning indicate smouldering emissions overnight may be particularly significant as pollutants accumulate in the nocturnal boundary layer. Substantial dry deposition could remove near surface aerosol and drive the observed Δaerosol:ΔCO. However, fluxes reported in the literature (Ahlm et al., 2010) are small compared to the number concentrations observed (Darbyshire et al., 2018) and thus we discount the role of dry deposition.

The average vertical distribution of pollutants in this study are similar to those from previous in situ and remote sensing observations in the region, despite temporal, geographic and instrumental sampling differences. This indicates driving processes are common throughout. The aerosol vertical profile is approximately vertical from the surface to a height of: 2.25 km (Huang et al., 2015; Table 2 therein), ~1.5 km (Bourgeois et al., 2015; Fig. 6 therein), ~2 km (Baars et al., 2012; Fig. 12 therein), ~1.5 km (Andreae et al., 2012; Fig. 6 therein), ~2 km (Marenco et al., 2016; Fig. 9 therein) or 1.5 - 3.5 km (this work, Fig. 8). Loadings reduce to near baseline values above ~4 km in all. Only in Andreae et al. (2012) have similar regionally averaged profiles of CO been presented. These exhibit a similar profile shape as here - greatest near the surface and reducing thereafter to a minima at ~4 km. This study therefore also demonstrated the same relationship of Δaerosol:ΔCO with altitude as observed here. Whilst studies displaying only a few profiles (e.g. Andreae et al., 1988, 2004; Chand et al., 2006; Pereira et al., 1996; Yokelson et al., 2007) may not mirror these average distributions, comparable profiles are present in our library of individual profiles (Sect S5,) indicating that our more extensive dataset is consistent with previous reports and captures variability between different studies.

4.2 Implications

We have observed a marked contrast in pollutant composition and vertical distribution from west to east across tropical South America which has not previously been identified. Given predicted 'savannisation' of the southern and eastern edges of the Amazon rainforest owing to climate change, deforestation and fire-climate feedbacks (Nobre et al., 2016) we recommend model analyses are carried out to assess the magnitude of these effects which may impact convective motions, cloud formation and regional dynamics.

The linkages between pollutants and atmospheric structure presented here reinforce the first order requirement for representation of realistic thermodynamics within models. This is currently a challenge for regional and global models, especially sub-grid convective mixing which drives the aerosol profile shape (Archer-Nicholls et al., 2016; Hong and Dudhia, 2012). For instance ECMWF ERA-Interim equivalent potential temperature profiles compare poorly to our measurements (Fig. 11) and those of Beck et al. (2013). These model fields are often used as boundary conditions for regional models and as such may introduce unrealistic thermodynamic structures and thus pollutant vertical distributions. Whilst the broad shape of horizontal wind shear from model output is captured on the individual profile basis, the fine structure present in observations is missing. Comparisons with ECMWF ERA-Interim and WRF output indicate this is the case for both global models and finer scale regional models. This may be problematic in accurately representing sub-grid processes, such as plume rise and convective mixing.

Following ignition a fire undergoes a period of more complete combustion, the flaming phase, a period of less complete combustion, the smouldering phase, and then a period of even less complete combustion, the residual smouldering phase. Based on our results we hypothesise these less prominent phases are potentially important in driving the observed Δaerosol:ΔCO profile. Aerosol rich emissions from the initial flaming phase will be lofted, whilst CO rich emissions from residual smouldering will be released near surface. Convective mixing will act to rebalance this contrast, although it remains

owing to the ubiquity of residual layers and plume injections aloft. Past satellite observations have suggested residual smouldering is a large source of CO and not fully captured by emissions inventories (Deeter et al., 2016; Pechony et al., 2013), which may be based on inappropriate emissions factors or arise from small fires outside the detection limit of active fire detection schemes (Giglio et al., 2016; Schroeder et al., 2008). Even if single fire-integrated emissions factors represent the

5 total pollution released, our results suggest their use may not always be appropriate in model simulations which draw results based on a realistic vertical distribution. For example aerosol-cloud and aerosol-radiation interactions, or surface air quality simulations. If emissions from flaming combustion are to be released at altitude, further exploration of the processes and variability in TSA is required. Archer-Nicholls et al. (2015) demonstrated how the parameterised Freitas et al. (2007) plume rise model calculated injection heights which were too high in TSA. Climatological distributions of plume injection heights,

10 which can prescribe model injection heights, show substantial diversity in TSA. The distributions derived by Marenco et al. (2016), consistent with plume heights in this study (Fig. S10), show injection heights at greater altitudes than those from CALIOP (Sofiev et al., 2013) and MISR (Fig. S11) satellite observations.

6 Conclusions

The vertical distribution of biomass burning pollutants regulates their subsequent horizontal distribution and thus the

15 magnitude of associated impacts on weather, climate and air quality. In tropical biomass burning regions, pollutant vertical distributions and their driving processes are poorly characterised. Here, a novel integrated analysis of individual profiles from research flights in tropical South America has helped reduce some of these uncertainties.

The thermodynamic structure of the lower troposphere was found to be critical in determining the pollutant vertical distribution on the local and regional scale. Pollutants were typically confined to the atmospheric boundary layer in either an

20 active or residual convective mixed layer. This was deeper in the east (~3 km) than west (~1.5 km) reflecting a regional contrast in soil moisture and surface insolation and as such significant differences in sensible and latent heat. Horizontal wind shear was important in advecting pollutants, inhibiting mixed layer growth and the vertical ascent of smoke plumes from fires. In order to accurately simulate the vertical and regional distribution of biomass burning pollution our results highlight not only the importance of capturing boundary layer dynamics and convection adequately, but also the release of pollutant plumes at

25 altitude.

During dry season conditions we observed a significant contrast in the pollutant haze composition between the western and eastern regions, which corresponded to different fire regimes. Whilst aerosol scattering coefficients of 120 Mm^{-1} and CO mixing ratios of ~310 ppb were similar, black carbon mass loadings were much greater in the east than west - 1.5 vs. 0.85 μg cm^{-3}. Cerrado burns in the east are more flaming, whilst those in the west, of primary/secondary forest and pasture land are

30 more smouldering (Hodgson et al., 2018). This discrepancy clearly merits future investigation in modelling studies to assess potential impacts on aerosol optical properties and their radiative effects.

Following the transition to wet season conditions in the west, fire activity declined and the observed concentration of black carbon mass, aerosol scattering coefficients and CO mixing ratios decreased. However, the ratios between these pollutants remained similar to ratios observed in the drier phase indicating little change to the composition of fire emissions despite the shift in meteorological conditions.

5   In the remote rainforest region of northern Amazonas state, significant concentrations of well mixed and thickly coated black carbon particles were observed in the lowermost 2 km and with comparatively low aerosol scattering coefficients. Trajectory analysis indicated origins from north-east Brazil where Cerrado fires were prevalent and, based on observations of Cerrado fires elsewhere, likely emit aerosol with a relatively high BC mass fractions. Given the high fire count and fire radiative power in this source fire region and the prevailing low level easterlies, the export of absorbing aerosol into the remote

10 central regions of Amazonia may commonly occur during the dry season.

In all regimes we observed an increasing contribution of pollutants from more flaming combustion with altitude – there is relatively more aerosol aloft and more CO near the surface. Typically there is no explicit representation in atmospheric models of emissions from only the residual smouldering stage, which would remain near the surface, nor those only from the flaming stage, which would also require transportation to an appropriate injection altitude. This may impede accurate predictions of

15 aerosol-radiation and aerosol-cloud interactions, in addition to air quality forecasts. Further enquiry is recommended to test the magnitude of these findings.

The results here may be applicable to other tropical biomass burning regions where observations of processes affecting pollutant vertical distributions are limited. Given the important impacts of biomass burning on meteorology, climate, air quality and ecosystem services, further vertically resolved observations of aerosol and trace gas pollutants are recommended.

20 **Data Availability**

All raw time series data used to derive the vertical profiles from the FAAM research aircraft are publicly available from the Centre for Environmental Data Analysis website (http://www.ceda.ac.uk/, last access: 31 August 2018). A direct links to the flight data records are given in the reference list (Facility for Airborne Atmospheric Measurements, Natural Environment Research Council, and Met Office, 2014). Raw active fire and Land use data used in the manuscript are available publicly

25 from NASA and ESA respectively (see Acknowledgements). Processed individual and averaged vertical profiles, data masks, plume composition, model output and satellite fields and are currently available on request from E. Darbyshire. Lidar data is available on request from F. Marenco (franco.marenco@metoffice.gov.uk).

Author Contributions

ED analysed the data and wrote the manuscript with the aid of WTM, HC, BJ, JFB and FM. WTM, JDA, DLiu, DLowe, SO'S, FM and KS provided additional data analysis support, including data processing and quality assurance. MJF, JD, KS and JFB operated aerosol instruments during the field campaign. SB operated gas phase instruments during the field campaign.

5   BJ, JMH, KML, PA and HC led the planning of the field campaign and were co-principal investigators on the SAMBBA project.

Competing Interests

The authors declare that they have no conflict of interest.

Special Issue Statement

10   This article is part of the special issue "South American Biomass Burning Analysis (SAMBBA)". It is not associated with a conference.

Acknowledgements

We would like to thank those involved in the SAMBBA project. This includes the Facility for Airborne Atmospheric Measurement (FAAM) and DirectFlight Ltd. who manage and operate the BAe-146-301 Atmospheric Research Aircraft
15   (ARA), which is jointly funded by the Natural Environment Research Council (NERC) and the Met Office. A number of institutions were involved in logistics, planning and support for the SAMBBA campaign: The Met Office, INPE, University of Sao Paulo and the Brazilian Ministry of Science and Technology. Moderate Resolution Imaging Spectroradiometer (MODIS) AOD data (MOD08_D3.051) and Tropical Rainfall Measuring Mission (TRMM) precipitation data were retrieved from the GIOVANNI online data system (http://disc.sci.gsfc.nasa.gov/giovanni), developed and maintained by the NASA
20   GES DISC. Active fire data was produced by the University of Maryland and acquired from the online Fire Information for Resource Management System (FIRMS; https://earthdata.nasa.gov/data/near-real-time-data/firms/abouts; specific product: MCD14ML). Land cover data was provided to the United Nations (UN) Land Cover Classification System by the ESA CCI Land Cover project (https://www.esa-landcover-cci.org/). ERA-Interim soil moisture, relative humidity, wind fields and temperature data was provided courtesy of ECMWF. We acknowledge those involved in the Multi-angle Imaging
25   SpectroRadiometer (MISR) Plume Height Project for analysis and provision of data. The lead author was supported by a NERC studentship NE/J500057/1 and NE/K500859/1, and the SAMBBA project by NERC grant NE/J010073/1.

References

Ahlm, L., Krejci, R., Nilsson, E. D., Mårtensson, E. M., Vogt, M. and Artaxo, P.: Emission and dry deposition of accumulation mode particles in the Amazon Basin, Atmos. Chem. Phys., 10(21), 10237–10253, doi:10.5194/acp-10-10237-2010, 2010.

Akagi, S. K., Yokelson, R. J., Wiedinmyer, C., Alvarado, M. J., Reid, J. S., Karl, T., Crounse, J. D. and Wennberg, P. O.: Emission factors for open and domestic biomass burning for use in atmospheric models, Atmos. Chem. Phys., 11(9), 4039–4072, doi:10.5194/acp-11-4039-2011, 2011.

Allan, J. D., Morgan, W. T., Darbyshire, E., Flynn, M. J., Williams, P. I., Oram, D. E., Artaxo, P., Brito, J., Lee, J. D. and Coe, H.: Airborne observations of IEPOX-derived isoprene SOA in the Amazon during SAMBBA, Atmos. Chem. Phys., 14(20), 11393–11407, doi:10.5194/acp-14-11393-2014, 2014.

Anderson, T. L. and Ogren, J. a.: Determining Aerosol Radiative Properties Using the TSI 3563 Integrating Nephelometer, Aerosol Sci. Technol., 29(1), 57–69, doi:10.1080/02786829808965551, 1998.

Anderson, T. L., Covert, D. S., Marshall, S. F., Laucks, M. L., Charlson, R. J., Waggoner, A. P., Ogren, J. A., Caldow, R., Holm, R. L., Quant, F. R., Sem, G. J., Wiedensohler, A., Ahlquist, N. A. and Bates, T. S.: Performance Characteristics of a High-Sensitivity, Three-Wavelength, Total Scatter/Backscatter Nephelometer, J. Atmos. Ocean. Technol., 13(5), 967–986, doi:10.1175/1520-0426(1996)013<0967:PCOAHS>2.0.CO;2, 1996.

Andreae, M. O., Browell, E. V., Garstang, M., Gregory, G. L., Harriss, R. C., Hill, G. F., Jacob, D. J., Pereira, M. C., Sachse, G. W., Setzer, A. W., Dias, P. L. S., Talbot, R. W., Torres, A. L. and Wofsy, S. C.: Biomass-burning emissions and associated haze layers over Amazonia, J. Geophys. Res., 93(D2), 1509, doi:10.1029/JD093iD02p01509, 1988.

Andreae, M. O., Rosenfeld, D., Artaxo, P., Costa, A. A., Frank, G. P., Longo, K. M. and Silva-Dias, M. A. F.: Smoking rain clouds over the Amazon., Science, 303(5662), 1337–42, doi:10.1126/science.1092779, 2004.

Andreae, M. O., Artaxo, P., Beck, V., Bela, M., Freitas, S., Gerbig, C., Longo, K., Munger, J. W., Wiedemann, K. T. and Wofsy, S. C.: Carbon monoxide and related trace gases and aerosols over the Amazon Basin during the wet and dry seasons, Atmos. Chem. Phys., 12(13), 6041–6065, doi:10.5194/acp-12-6041-2012, 2012.

Archer-Nicholls, S., Lowe, D., Darbyshire, E., Morgan, W. T., Bela, M. M., Pereira, G., Trembath, J., Kaiser, J. W., Longo, K. M., Freitas, S. R., Coe, H. and McFiggans, G.: Characterising Brazilian biomass burning emissions using WRF-Chem with MOSAIC sectional aerosol, Geosci. Model Dev., 8(3), 549–577, doi:10.5194/gmd-8-549-2015, 2015.

Archer-Nicholls, S., Lowe, D., Schultz, D. M. and McFiggans, G.: Aerosol–radiation–cloud interactions in a regional coupled model: the effects of convective parameterisation and resolution, Atmos. Chem. Phys., 16(9), 5573–5594, doi:10.5194/acp-16-5573-2016, 2016.

Artaxo, P., Rizzo, L. V, Brito, J. F., Barbosa, H. M. J., Arana, A., Sena, E. T., Cirino, G. G., Bastos, W., Martin, S. T. and Andreae, M. O.: Atmospheric aerosols in Amazonia and land use change: from natural biogenic to biomass burning conditions, Faraday Discuss., 165(0), 203–235, doi:10.1039/C3FD00052D, 2013.

Baars, H., Ansmann, A., Althausen, D., Engelmann, R., Heese, B., Müller, D., Artaxo, P., Paixao, M., Pauliquevis, T. and

Souza, R.: Aerosol profiling with lidar in the Amazon Basin during the wet and dry season, J. Geophys. Res. Atmos., 117, D21201, doi:10.1029/2012JD018338, 2012.

Baumgardner, D., Kok, G. and Raga, G.: Warming of the Arctic lower stratosphere by light absorbing particles, Geophys. Res. Lett., 31(6), doi:10.1029/2003GL018883, 2004.

Beck, V., Gerbig, C., Koch, T., Bela, M. M., Longo, K. M., Freitas, S. R., Kaplan, J. O., Prigent, C., Bergamaschi, P. and Heimann, M.: WRF-Chem simulations in the Amazon region during wet and dry season transitions: Evaluation of methane models and wetland inundation maps, Atmos. Chem. Phys., 13(16), 7961–7982, doi:10.5194/acp-13-7961-2013, 2013.

Boucher, O., Randall, D., Artaxo, P., Bretherton, C., Feingold, G., Forster, P., Kerminen, V.-M., Kondo, Y., Liao, H., Lohmann, U., Rasch, P., Satheesh, S. K., Sherwood, S., Stevens, B. and Zhang, X. Y.: Clouds and Aerosols, in Climate Change 2013: The Physical Science Basis. Contribution of Working Group I to the Fifth Assessment Report of the Intergovernmental Panel on Climate Change, pp. 571–657, Cambridge University Press, Cambridge, United Kingdom and New York, NY, USA., 2013.

Bourgeois, Q., Ekman, A. M. L. and Krejci, R.: Aerosol transport over the Andes from the Amazon Basin to the remote Pacific Ocean: A multiyear CALIOP assessment, J. Geophys. Res. Atmos., 120(16), 8411–8425, doi:10.1002/2015JD023254, 2015.

Brito, J., Rizzo, L. V., Morgan, W. T., Coe, H., Johnson, B., Haywood, J., Longo, K., Freitas, S., Andreae, M. O. and Artaxo, P.: Ground-based aerosol characterization during the South American Biomass Burning Analysis (SAMBBA) field experiment, Atmos. Chem. Phys., 14(22), 12069–12083, doi:10.5194/acp-14-12069-2014, 2014.

Chand, D., Guyon, P., Artaxo, P., Schmid, O., Frank, G. P., Rizzo, L. V., Mayol-Bracero, O. L., Gatti, L. V. and Andreae, M. O.: Optical and physical properties of aerosols in the boundary layer and free troposphere over the Amazon Basin during the biomass burning season, Atmos. Chem. Phys., 6(10), 2911–2925, doi:10.5194/acp-6-2911-2006, 2006.

Darbyshire, E. Morgan, W. T., Allan, J. D., Liu, D., Flynn, M. J., Dorsey, J. R., O'Shea, S. J., Trembath, J., Johnson, B. T., Szpek, K., Haywood, J. M., Brito, J. F., Artaxo, P., Longo, K. M., Coe, H.: Contrasting aerosol heating from biomass burning haze between deforestation and Cerrado regions of tropical South America, as derived from airborne composition measurements (in preperation)

Deeter, M. N., Martínez-Alonso, S., Gatti, L. V., Gloor, M., Miller, J. B., Domingues, L. G. and Correia, C. S. C.: Validation and analysis of MOPITT CO observations of the Amazon Basin, Atmos. Meas. Tech., 9(8), 3999–4012, doi:10.5194/amt-9-3999-2016, 2016.

Edwards, D. P., Emmons, L. K., Gille, J. C., Chu, A., Attié, J.-L., Giglio, L., Wood, S. W., Haywood, J., Deeter, M. N., Massie, S. T., Ziskin, D. C. and Drummond, J. R.: Satellite-observed pollution from Southern Hemisphere biomass burning, J. Geophys. Res., 111(D14), D14312, doi:10.1029/2005JD006655, 2006.

Feingold, G., Jiang, H. and Harrington, J. Y.: On smoke suppression of clouds in Amazonia, Geophys. Res. Lett., 32(2), L02804, doi:10.1029/2004GL021369, 2005.

Ferek, R. J., Reid, J. S., Hobbs, P. V, Blake, D. R. and Liousse, C.: Emission factors of hydrocarbons, halocarbons, trace gases and particles from biomass burning in Brazil, J. Geophys. Res. Atmos., 103(D24), 32107–32118, doi:10.1029/98JD00692, 1998.

Freitas, S. R., Longo, K. M. and Andreae, M. O.: Impact of including the plume rise of vegetation fires in numerical simulations of associated atmospheric pollutants, Geophys. Res. Lett., 33(17), 1–5, doi:10.1029/2006GL026608, 2006.

Freitas, S. R., Longo, K. M., Chatfield, R., Latham, D., Silva Dias, M. A. F., Andreae, M. O., Prins, E., Santos, J. C., Gielow, R. and Carvalho, J. A.: Including the sub-grid scale plume rise of vegetation fires in low resolution atmospheric transport models, Atmos. Chem. Phys., 7(13), 3385–3398, doi:10.5194/acp-7-3385-2007, 2007.

Freitas, S. R., Longo, K. M., Silva Dias, M. A. F., Chatfield, R., Silva Dias, P., Artaxo, P., Andreae, M. O., Grell, G., Rodrigues, L. F., Fazenda, A. and Panetta, J.: The Coupled Aerosol and Tracer Transport model to the Brazilian developments on the Regional Atmospheric Modeling System (CATT-BRAMS) – Part 1: Model description and evaluation, Atmos. Chem. Phys., 9(8), 2843–2861, doi:10.5194/acp-9-2843-2009, 2009.

Freitas, S. R., Longo, K. M., Trentmann, J. and Latham, D.: Technical Note: Sensitivity of 1-D smoke plume rise models to the inclusion of environmental wind drag, Atmos. Chem. Phys., 10(2), 585–594, doi:10.5194/acp-10-585-2010, 2010.

Gerbig, C., Schmitgen, S., Kley, D., Volz-Thomas, A., Dewey, K. and Haaks, D.: An improved fast-response vacuum-UV resonance fluorescence CO instrument, J. Geophys. Res. Atmos., 104(D1), 1699–1704, doi:10.1029/1998JD100031, 1999.

Giglio, L., Csiszar, I. and Justice, C. O.: Global distribution and seasonality of active fires as observed with the Terra and Aqua Moderate Resolution Imaging Spectroradiometer (MODIS) sensors, J. Geophys. Res. Biogeosciences, 111(G2), n/a-n/a, doi:10.1029/2005JG000142, 2006.

Giglio, L., Schroeder, W. and Justice, C. O.: The collection 6 MODIS active fire detection algorithm and fire products, Remote Sens. Environ., 178, 31–41, doi:10.1016/j.rse.2016.02.054, 2016.

Graham, E. a, Mulkey, S. S., Kitajima, K., Phillips, N. G. and Wright, S. J.: Cloud cover limits net CO2 uptake and growth of a rainforest tree during tropical rainy seasons, Proc. Natl. Acad. Sci., 100(2), 572–576, doi:10.1073/pnas.0133045100, 2003.

Gregory, G. L., Browell, E. V. and Warren, L. S.: Boundary layer ozone: An airborne survey above the Amazon Basin, J. Geophys. Res., 93(D2), 1452–1468, doi:10.1029/JD093iD02p01452, 1988.

Hodgson, A. K., Morgan, W. T., O'Shea, S., Bauguitte, S., Allan, J. D., Darbyshire, E., Flynn, M. J., Liu, D., Lee, J., Johnson, B., Haywood, J. M., Longo, K. M., Artaxo, P. E. and Coe, H.: Near-field emission profiling of tropical forest and Cerrado fires in Brazil during SAMBBA 2012, Atmos. Chem. Phys., 18(8), 5619–5638, doi:10.5194/acp-18-5619-2018, 2018.

Hong, S.-Y. and Dudhia, J.: Next-Generation Numerical Weather Prediction: Bridging Parameterization, Explicit Clouds, and Large Eddies, Bull. Am. Meteorol. Soc., 93(1), ES6-ES9, doi:10.1175/2011BAMS3224.1, 2012.

Huang, J., Guo, J., Wang, F., Liu, Z., Jeong, M., Yu, H. and Zhang, Z.: CALIPSO inferred most probable heights of global dust and smoke layers, J. Geophys. Res. Atmos., 120(10), 5085–5100, doi:10.1002/2014JD022898, 2015.

Johnson, B. T., Haywood, J. M., Langridge, J. M., Darbyshire, E., Morgan, W. T., Szpek, K., Brooke, J. K., Marenco, F., Coe, H., Artaxo, P., Longo, K. M., Mulcahy, J. P., Mann, G. W., Dalvi, M. and Bellouin, N.: Evaluation of biomass burning aerosols in the HadGEM3 climate model with observations from the SAMBBA field campaign, Atmos. Chem. Phys., 16(22), 14657–14685, doi:10.5194/acp-16-14657-2016, 2016.

Koffi, B., Schulz, M., Bréon, F. M., Griesfeller, J., Winker, D., Balkanski, Y., Bauer, S., Berntsen, T., Chin, M., Collins, W. D., Dentener, F., Diehl, T., Easter, R., Ghan, S., Ginoux, P., Gong, S., Horowitz, L. W., Iversen, T., Kirkevg, A., Koch, D., Krol, M., Myhre, G., Stier, P. and Takemura, T.: Application of the CALIOP layer product to evaluate the vertical distribution of aerosols estimated by global models: AeroCom phase I results, J. Geophys. Res. Atmos., 117(10), 1–26, doi:10.1029/2011JD016858, 2012.

Kolusu, S. R., Marsham, J. H., Mulcahy, J., Johnson, B., Dunning, C., Bush, M. and Spracklen, D. V.: Impacts of Amazonia biomass burning aerosols assessed from short-range weather forecasts, Atmos. Chem. Phys., 15(21), 12251–12266, doi:10.5194/acp-15-12251-2015, 2015.

Kotchenruther, R. A. and Hobbs, P. V: Humidification factors of aerosols from biomass burning in Brazil, J. Geophys. Res. Atmos., 103(D24), 32081–32089, doi:10.1029/98JD00340, 1998.

Liu, D., Allan, J. D., Young, D. E., Coe, H., Beddows, D., Fleming, Z. L., Flynn, M. J., Gallagher, M. W., Harrison, R. M., Lee, J., Prevot, A. S. H., Taylor, J. W., Yin, J., Williams, P. I. and Zotter, P.: Size distribution, mixing state and source apportionment of black carbon aerosol in London during winter time, Atmos. Chem. Phys., 14(18), 10061–10084, doi:10.5194/acp-14-10061-2014, 2014.

Marenco, F., Johnson, B., Langridge, J. M., Mulcahy, J., Benedetti, A., Remy, S., Jones, L., Szpek, K., Haywood, J., Longo, K. and Artaxo, P.: On the vertical distribution of smoke in the Amazonian atmosphere during the dry season, Atmos. Chem. Phys., 16(4), 2155–2174, doi:10.5194/acp-16-2155-2016, 2016.

McBeath, K.: The use of aircraft for meteorological research in the United Kingdom, Meteorol. Appl., 21(1), 105–116, doi:10.1002/met.1448, 2014.

McMeeking, G. R., Hamburger, T., Liu, D., Flynn, M., Morgan, W. T., Northway, M., Highwood, E. J., Krejci, R., Allan, J. D., Minikin, A. and Coe, H.: Black carbon measurements in the boundary layer over western and northern Europe, Atmos. Chem. Phys., 10(19), 9393–9414, doi:10.5194/acp-10-9393-2010, 2010.

Müller, T., Laborde, M., Kassell, G. and Wiedensohler, A.: Design and performance of a three-wavelength LED-based total scatter and backscatter integrating nephelometer, Atmos. Meas. Tech., 4(6), 1291–1303, doi:10.5194/amt-4-1291-2011, 2011.

Nobre, C. A., Sampaio, G., Borma, L. S., Castilla-Rubio, J. C., Silva, J. S. and Cardoso, M.: Land-use and climate change risks in the Amazon and the need of a novel sustainable development paradigm, Proc. Natl. Acad. Sci., 113(39), 10759–10768, doi:10.1073/pnas.1605516113, 2016.

O'Shea, S. J., Allen, G., Gallagher, M. W., Bauguitte, S. J.-B., Illingworth, S. M., Le Breton, M., Muller, J. B. a., Percival, C. J., Archibald, a. T., Oram, D. E., Parrington, M., Palmer, P. I. and Lewis, a. C.: Airborne observations of trace gases

over boreal Canada during BORTAS: campaign climatology, air mass analysis and enhancement ratios, Atmos. Chem. Phys., 13(24), 12451–12467, doi:10.5194/acp-13-12451-2013, 2013.

Paugam, R., Wooster, M., Freitas, S. and Val Martin, M.: A review of approaches to estimate wildfire plume injection height within large-scale atmospheric chemical transport models, Atmos. Chem. Phys., 16(2), 907–925, doi:10.5194/acp-16-907-2016, 2016.

Pechony, O., Shindell, D. T. and Faluvegi, G.: Direct top-down estimates of biomass burning CO emissions using TES and MOPITT versus bottom-up GFED inventory, J. Geophys. Res. Atmos., 118(14), 8054–8066, doi:10.1002/jgrd.50624, 2013.

Pereira, E. B., Setzer, A. W., Gerab, F., Artaxo, P. E., Pereira, M. C. and Monroe, G.: Airborne measurements of aerosols from burning biomass in Brazil related to the TRACE A experiment, J. Geophys. Res., 101(D19), 23983–23992, doi:10.1029/96JD00098, 1996.

Pereira, G., Siqueira, R., Rosário, N. E., Longo, K. L., Freitas, S. . R., Cardozo, F. S., Kaiser, J. W. and Wooster, M. J.: Assessment of fire emission inventories during the South American Biomass Burning Analysis (SAMBBA) experiment, Atmos. Chem. Phys., 16(11), 6961–6975, doi:10.5194/acp-16-6961-2016, 2016.

Prins, E. M., Feltz, J. M., Menzel, W. P. and Ward, D. E.: An overview of GOES-8 diurnal fire and smoke results for SCAR-B and 1995 fire season in South America, J. Geophys. Res., 103(D24), 31821, doi:10.1029/98JD01720, 1998.

Rap, A., Spracklen, D. V, Mercado, L., Reddington, C. L., Haywood, J. M., Ellis, R. J., Phillips, O. L., Artaxo, P., Bonal, D., Restrepo Coupe, N. and Butt, N.: Fires increase Amazon forest productivity through increases in diffuse radiation, Geophys. Res. Lett., 42(11), 4654–4662, doi:10.1002/2015GL063719, 2015.

Reddington, C. L., Butt, E. W., Ridley, D. A., Artaxo, P., Morgan, W. T., Coe, H. and Spracklen, D. V.: Air quality and human health improvements from reductions in deforestation-related fire in Brazil, Nat. Geosci., 8(10), 768–771, doi:10.1038/ngeo2535, 2015.

Reddington, C. L., Spracklen, D. V, Artaxo, P., Ridley, D., Rizzo, L. V and Arana, A.: Analysis of particulate emissions from tropical biomass burning using a global aerosol model and long-term surface observations, Atmos. Chem. Phys. Discuss., (November 2015), 1–49, doi:10.5194/acp-2015-967, 2016.

Reddington, C. L., Morgan, W. T., Darbyshire, E., Brito, J., Coe, H., Artaxo, P., Marsham, J., Spracklen, D. V.: Biomass burning aerosol over the Amazon: analysis of aircraft, surface and satellite observations using a global aerosol model, Atmos. Chem. Phys (in review)

Rizzo, L. V., Artaxo, P., Müller, T., Wiedensohler, A., Paixão, M., Cirino, G. G., Arana, A., Swietlicki, E., Roldin, P., Fors, E. O., Wiedemann, K. T., Leal, L. S. M. and Kulmala, M.: Long term measurements of aerosol optical properties at a primary forest site in Amazonia, Atmos. Chem. Phys., 13(5), 2391–2413, doi:10.5194/acp-13-2391-2013, 2013.

Ross, J. L., Hobbs, P. V and Holben, B.: Radiative characteristics of regional hazes dominated by smoke from biomass burning in Brazil: Closure tests and direct radiative forcing, J. Geophys. Res. Atmos., 103(D24), 31925–31941, doi:10.1029/97JD03677, 1998.

Sachse, G. W., Harriss, R. C., Fishman, J., Hill, G. F. and Cahoon, D. R.: Carbon monoxide over the Amazon Basin during the 1985 dry season, J. Geophys. Res., 93(D2), 1422, doi:10.1029/JD093iD02p01422, 1988.

Schroeder, W., Prins, E., Giglio, L., Csiszar, I., Schmidt, C., Morisette, J. and Morton, D.: Validation of GOES and MODIS active fire detection products using ASTER and ETM+ data, Remote Sens. Environ., 112, 2711–2726, doi:10.1016/j.rse.2008.01.005, 2008.

Schwarz, J. P., Gao, R. S., Spackman, J. R., Watts, L. A., Thomson, D. S., Fahey, D. W., Ryerson, T. B., Peischl, J., Holloway, J. S., Trainer, M., Frost, G. J., Baynard, T., Lack, D. A., de Gouw, J. A., Warneke, C. and Del Negro, L. A.: Measurement of the mixing state, mass, and optical size of individual black carbon particles in urban and biomass burning emissions, Geophys. Res. Lett., 35(13), L13810, doi:10.1029/2008GL033968, 2008.

Shiraiwa, M., Kondo, Y., Moteki, N., Takegawa, N., Sahu, L. K., Takami, A., Hatakeyama, S., Yonemura, S. and Blake, D. R.: Radiative impact of mixing state of black carbon aerosol in Asian outflow, J. Geophys. Res., 113(D24), D24210, doi:10.1029/2008JD010546, 2008.

Sofiev, M., Vankevich, R., Ermakova, T. and Hakkarainen, J.: Global mapping of maximum emission heights and resulting vertical profiles of wildfire emissions, Atmos. Chem. Phys., 13(14), 7039–7052, doi:10.5194/acp-13-7039-2013, 2013.

Stephens, M., Turner, N. and Sandberg, J.: Particle identification by laser-induced incandescence in a solid-state laser cavity, Appl. Opt., 42(19), 3726, doi:10.1364/AO.42.003726, 2003.

Stull, R. B.: A Fair-Weather Cumulus Cloud Classification Scheme for Mixed-Layer Studies, J. Clim. Appl. Meteorol., 24(1), 49–56, doi:10.1175/1520-0450(1985)024<0049:AFWCCC>2.0.CO;2, 1985.

Tao, W.-K., Chen, J.-P., Li, Z., Wang, C. and Zhang, C.: Impact of aerosols on convective clouds and precipitation, Rev. Geophys., 50(2), RG2001, doi:10.1029/2011RG000369, 2012.

Taylor, J. W., Allan, J. D., Allen, G., Coe, H., Williams, P. I., Flynn, M. J., Le Breton, M., Muller, J. B. a., Percival, C. J., Oram, D., Forster, G., Lee, J. D., Rickard, a. R. and Palmer, P. I.: Size-dependent wet removal of black carbon in Canadian biomass burning plumes, Atmos. Chem. Phys. Discuss., 14(13), 19469–19513, doi:10.5194/acpd-14-19469-2014, 2014.

Taylor, J. W., Allan, J. D., Liu, D., Flynn, M., Weber, R., Zhang, X., Lefer, B. L., Grossberg, N., Flynn, J. and Coe, H.: Assessment of the sensitivity of core / shell parameters derived using the single-particle soot photometer to density and refractive index, Atmos. Meas. Tech., 8(4), 1701–1718, doi:10.5194/amt-8-1701-2015, 2015.

Trembath, J. A.: Airborne CCN Measurements, Ph.D. thesis, Faculty of Engineering and Physical Sciences, University of Manchester, UK., 2013.

Yokelson, R. J., Karl, T., Artaxo, P., Blake, D. R., Christian, T. J., Griffith, D. W. T., Guenther, A. and Hao, W. M.: The Tropical Forest and Fire Emissions Experiment: overview and airborne fire emission factor measurements, Atmos. Chem. Phys., 7(19), 5175–5196, doi:10.5194/acp-7-5175-2007, 2007.

Zarzycki, C. M. and Bond, T. C.: How much can the vertical distribution of black carbon affect its global direct radiative forcing?, Geophys. Res. Lett., 37(20), 1–6, doi:10.1029/2010GL044555, 2010.
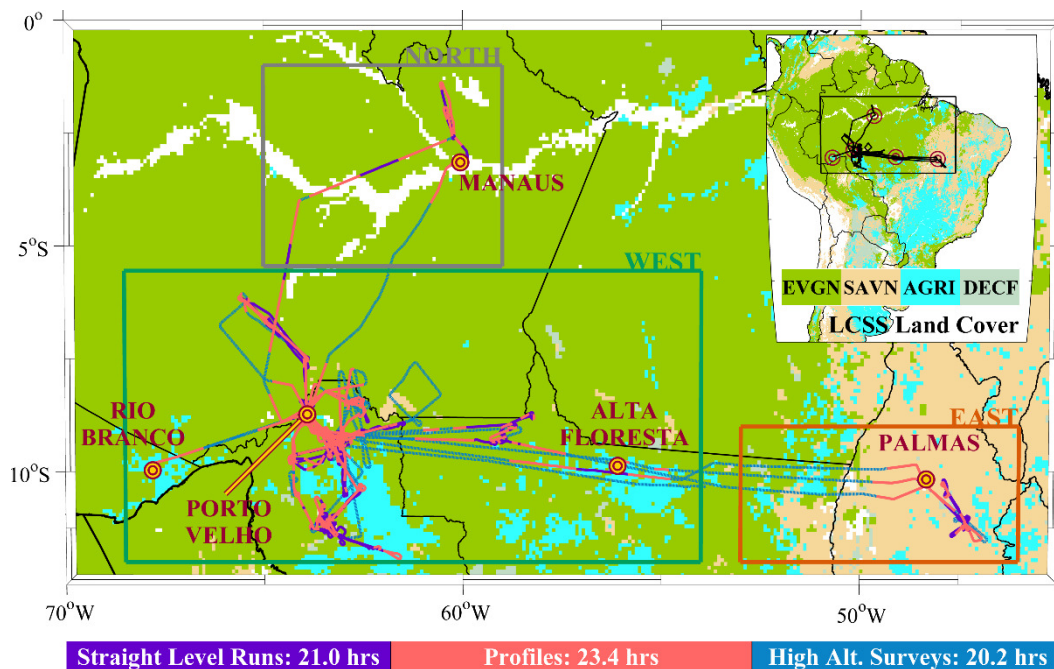
Figure 1. SAMBBA operational domain with flight tracks coloured by basic aircraft operation. 2012 land use based on a simplification of the UN Land Cover Classification System (LCCS) classification as described in the supplementary information: evergreen forest (EVGN), savanna (SAVN), deciduous forest (DECF) and agricultural land (AGRI).
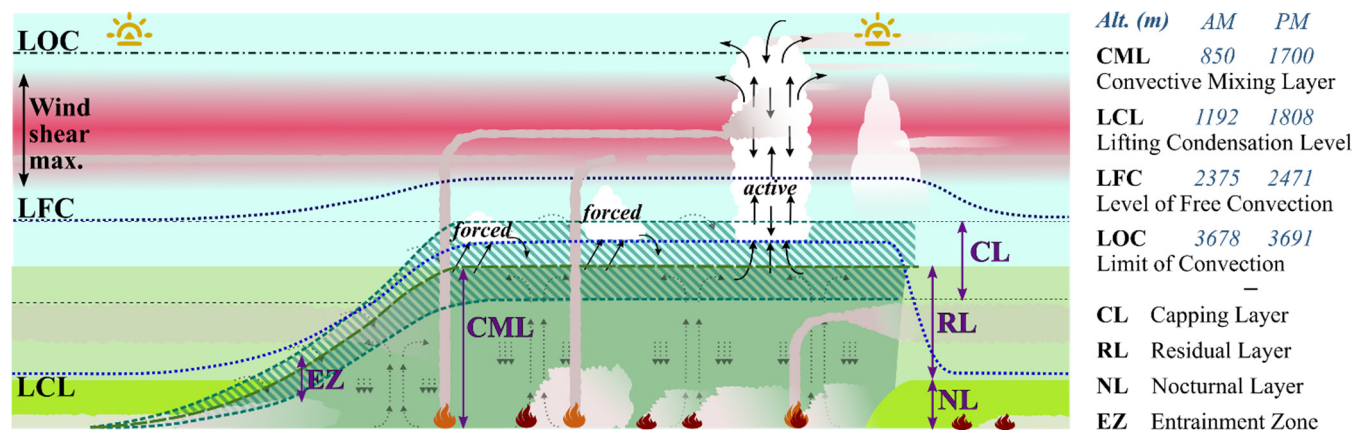
Figure 2. Schematic of the typical diurnal development of the convective boundary layer. This is based on visual and automated analysis of individual profiles and, for the nocturnal period outside our sampling times, previous tropical boundary layer literature. Red flame symbols indicate more smouldering fires and orange symbols more flaming combustion.
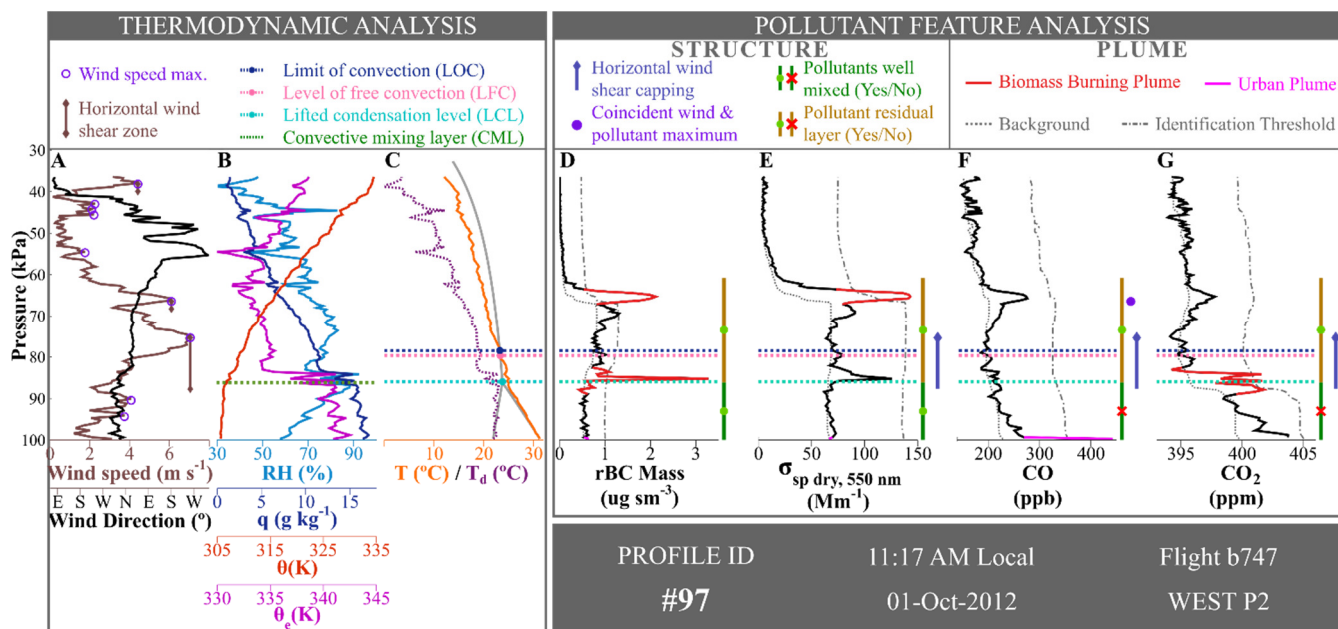
Figure 3. Individual profile #97, from flight b747 (01/10/2012) near Porto Velho in Rondônia state. From left to right are the vertical profiles of (A) wind speed and direction, (B) relative humidity (RH), specific humidity (q), potential temperature (θ) and equivalent potential temperature (θe), (C) temperature (T) and dew point temperature (Td) on a skew-T log-P scale, (D) refractory black carbon (rBC) mass, (E) aerosol scattering coefficient (550 nm), (F) CO and (G) CO2 mixing ratios. Thermodynamic features are illustrated in panels A-C (see Sect. 3.1). Pollutant feature analysis is illustrated in panels D-G (see Sect. 3.2).
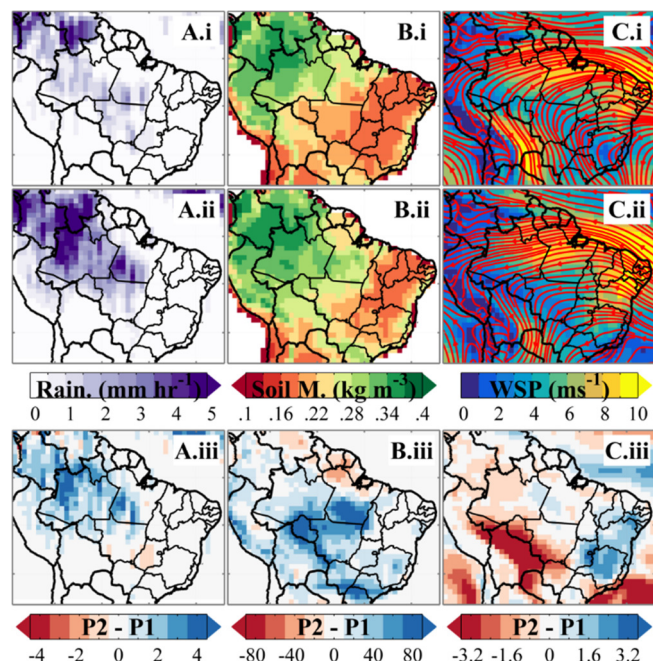
Figure 4. Precipitation (A), soil moisture (B) and 850 hPa wind speed and flowlines (C) during meteorological phases 1 (i, dry season) and 2 (ii, dry-wet transition season) and the difference between the two periods (iii). Precipitation is derived from TRMM measurements. The soil moisture and wind speed products are derived from ECMWF Era-Interim product.
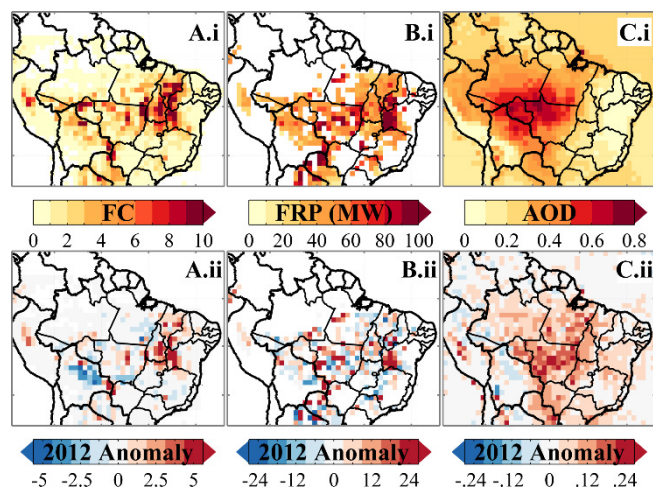
Figure 5. September 2008-2017 median total fire count (FC; A) and fire radiative power (FRP; B) from MODIS active fire detections, calculated over a 1° grid. The FC scale is divided by 100 for figure clarity. September 2008-2017 median aerosol optical depth (AOD; C) from MODIS 1° product. The 2012 anomaly for each of these fields is illustrated in panels (ii).
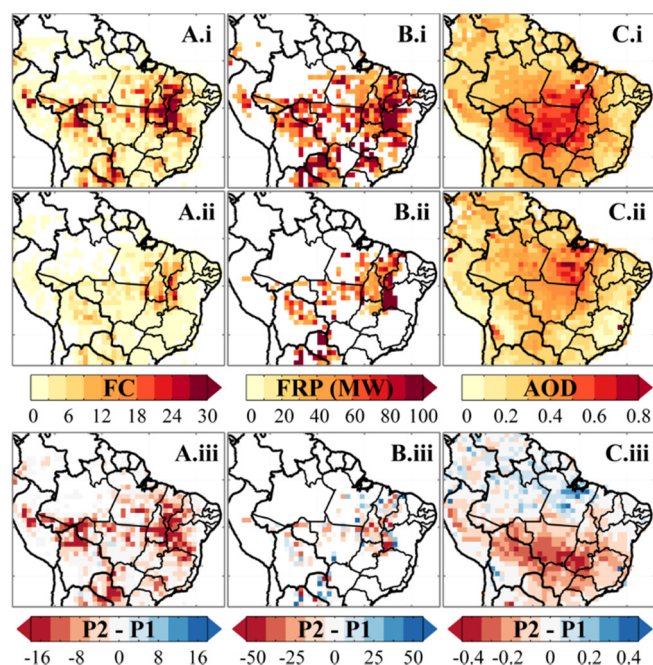
Figure 6. Meteorological phases 1 (i; dry season) and 2 (ii; dry-wet transition) median total fire count (FC; A) and fire radiative power (FRP; B) from MODIS active fire detections, calculated over a 1° grid. Meteorological phases 1 (i; dry season) and 2 (ii; dry-wet transition) median aerosol optical depth (AOD; C) from MODIS 1° product. The difference between these periods is illustrated in panels (iii).
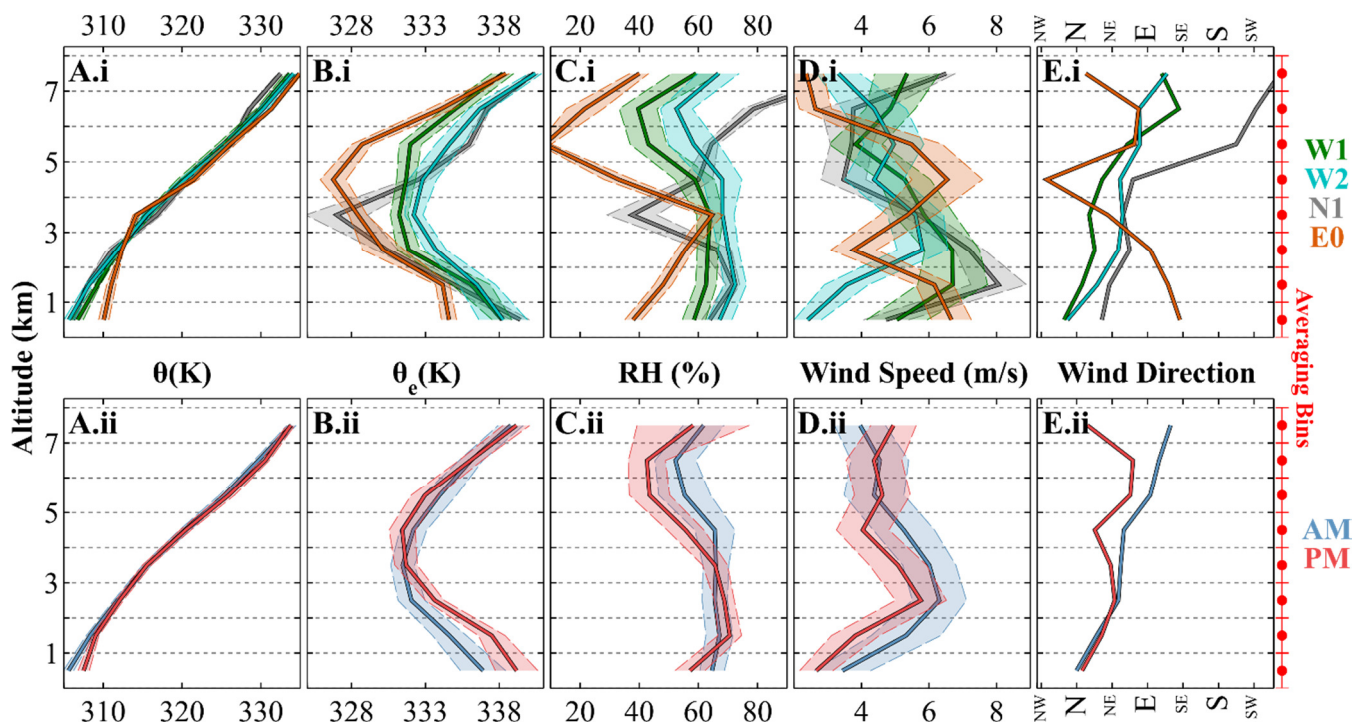
Figure 7. Median pollutant profiles averaged over the different regimes (top panels) and time of day (bottom panels, includes data from all regimes). Lighter shading represents the median absolute deviation.
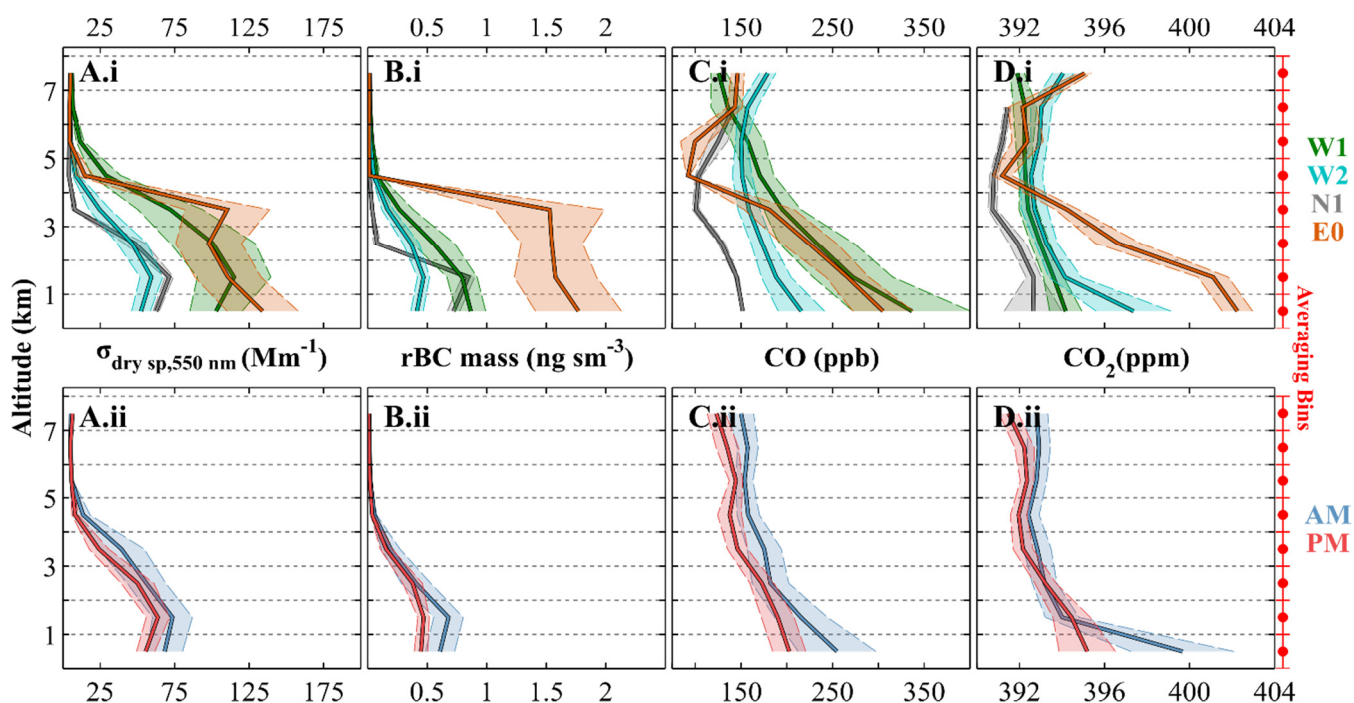
Figure 8. Median pollutant profiles averaged over the different regimes (top panels) and time of day (bottom panels, includes data from all regimes). Lighter shading represents the median absolute deviation. Note, σ_{sp_dry} is reported at standard temperature, standard pressure and 30% RH and hence the column AOD cannot be derived from these profiles.
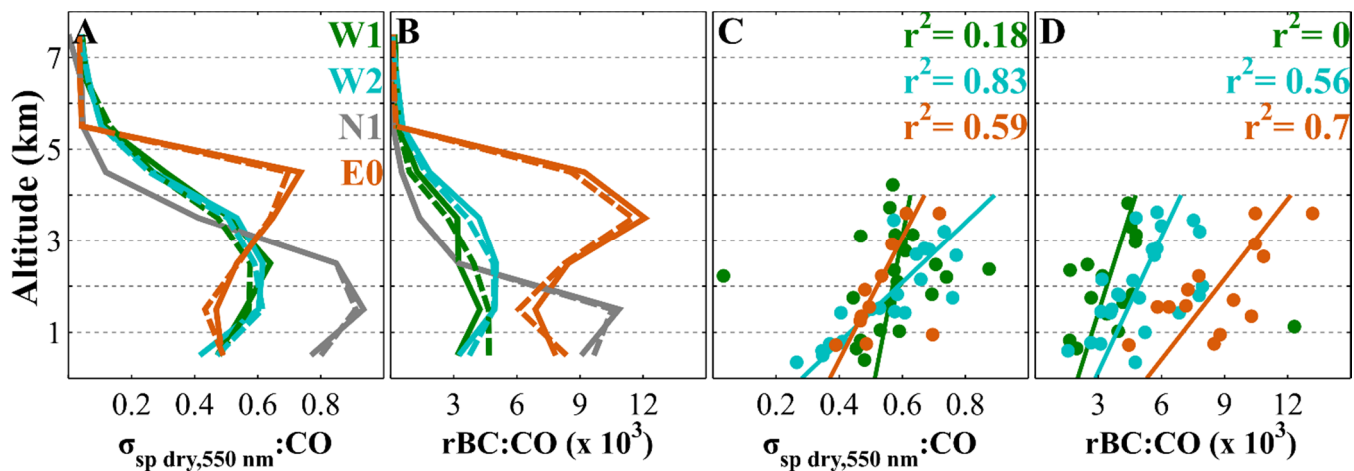
5   **Figure 9. σ_{sp_dry}:CO and rBC:CO enhancement profiles for each regime (A,B), and of plumes (C,D). Profile enhancements calculated from data minus the regime 5th percentile. Ratios reported for pollutants at ambient temperature and pressure. Solid (dashed) line represents averages with (without) plumes included. Plume enhancements calculated from plume integrated values above the local background (moving 5th percentile, i.e. brown baseline Fig. 3) only when the two pollutants are well correlated (Pearson's r > 0.5).**
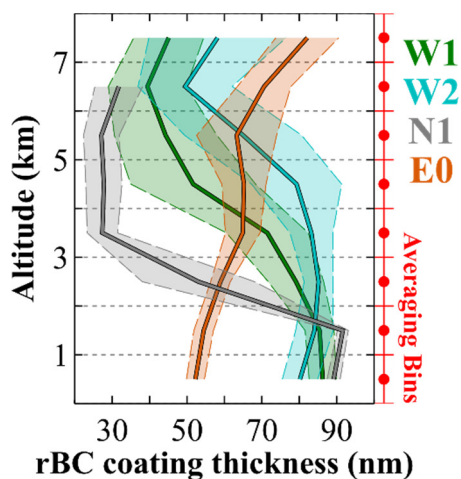
10   **Figure 10. Regime median profiles of black carbon coating thickness. Lighter shading represents the median absolute deviation.**
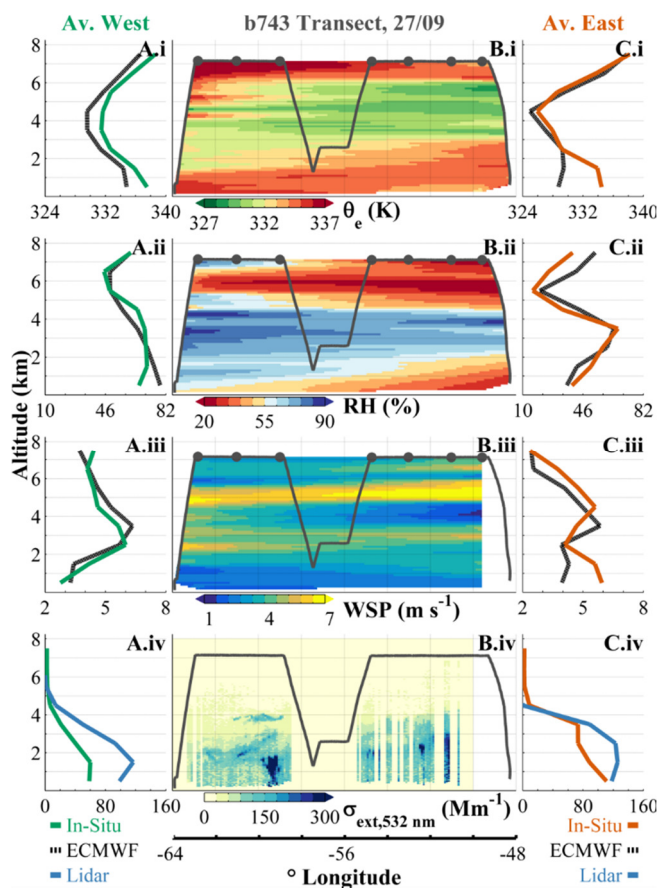
Figure 11. Thermodynamic and aerosol parameters averaged (median) across all western (A) and eastern flights (C) and across an afternoon east-west transect (B; flight b743). Measured equivalent potential temperature (i), relative humidity (ii) and horizontal wind speed (iii) is presented alongside ECMWF Reanalysis data (A,C) extracted along flight paths. The thermodynamic curtains (B.i-iii) represent linearly interpolated aircraft (grey line) and dropsonde (grey dots) profiles. The curtain of the lidar extinction coefficient at 532 nm (B.iv) is reproduced from Marenco et al., (2016) scaled from 355nm using a scaling factor of 0.57 following Marenco et al., (2014). σ_{sp} at ambient temperature and pressure is compared against the lidar extinction coefficient (A,C.iv) averaged over a similar region (Fig. S6).